

## Influence of pre-oxidation on filamentary carbon deposition on 20Cr25Ni stainless steel

Ding, Rengen; Taylor, Mary; Chiu, Yu-Lung; Smith, Neal; Mowforth, Clive; Evans, Hugh

DOI:

[10.1007/s11085-019-09891-4](https://doi.org/10.1007/s11085-019-09891-4)

License:

Creative Commons: Attribution (CC BY)

*Document Version*

Publisher's PDF, also known as Version of record

*Citation for published version (Harvard):*

Ding, R, Taylor, M, Chiu, Y-L, Smith, N, Mowforth, C & Evans, H 2019, 'Influence of pre-oxidation on filamentary carbon deposition on 20Cr25Ni stainless steel', *Oxidation of Metals*, vol. 91, no. 5-6, pp. 589-607.  
<https://doi.org/10.1007/s11085-019-09891-4>

[Link to publication on Research at Birmingham portal](#)

### **Publisher Rights Statement:**

Ding, R., Taylor, M.P., Chiu, Y.L. et al. *Oxid Met* (2019) 91: 589. <https://doi.org/10.1007/s11085-019-09891-4>

### **General rights**

Unless a licence is specified above, all rights (including copyright and moral rights) in this document are retained by the authors and/or the copyright holders. The express permission of the copyright holder must be obtained for any use of this material other than for purposes permitted by law.

- Users may freely distribute the URL that is used to identify this publication.
- Users may download and/or print one copy of the publication from the University of Birmingham research portal for the purpose of private study or non-commercial research.
- User may use extracts from the document in line with the concept of 'fair dealing' under the Copyright, Designs and Patents Act 1988 (?)
- Users may not further distribute the material nor use it for the purposes of commercial gain.

Where a licence is displayed above, please note the terms and conditions of the licence govern your use of this document.

When citing, please reference the published version.

### **Take down policy**

While the University of Birmingham exercises care and attention in making items available there are rare occasions when an item has been uploaded in error or has been deemed to be commercially or otherwise sensitive.

If you believe that this is the case for this document, please contact [UBIRA@lists.bham.ac.uk](mailto:UBIRA@lists.bham.ac.uk) providing details and we will remove access to the work immediately and investigate.



# Influence of Pre-oxidation on Filamentary Carbon Deposition on 20Cr25Ni Stainless Steel

R. Ding<sup>1</sup> · M. P. Taylor<sup>1</sup> · Y. L. Chiu<sup>1</sup> · N. Smith<sup>2</sup> · C. W. Mowforth<sup>2</sup> · H. E. Evans<sup>1</sup>

Received: 27 July 2018  
© The Author(s) 2019

## Abstract

The results of a pre-oxidation heat treatment at 930 °C in Ar/H<sub>2</sub>/H<sub>2</sub>O environments on a Si-bearing Nb-stabilised 20Cr25Ni austenitic steel are presented. The heat treatment was conducted under low  $pO_2$ , achieved by the introduction of controlled amounts of moisture into the gas. The atmosphere promoted the formation of a continuous, dense, adherent, protective surface scale composed of Cr<sub>2</sub>O<sub>3</sub> and MnCr<sub>2</sub>O<sub>4</sub> with a thin Si-rich oxide at the oxide alloy interface. Samples with different oxide layer thicknesses were produced and further exposed at 700 °C, to a gas of nominal composition CO<sub>2</sub>/1%CO/1000 vpm C<sub>2</sub>H<sub>4</sub> for 4 h. This gas mixture has a carbon activity greater than unity and readily forms filamentary carbon on the non-pre-oxidised alloy. This is catalysed by nickel particles formed intrinsically from the alloy during the early stages of oxidation of the unprotected surface. The oxide layers produced, as a result of the pre-oxidation process, could suppress carbon deposition onto the alloy; a significant reduction in carbon deposit was noted with an oxide of 125 nm thickness, and no deposit was found on the sample with an oxide thickness of 380 nm. The depth of depletion of chromium from the alloy correlated with the thickness of the oxide formed during the pre-oxidation heat treatment, but the chromium concentration at the oxide/metal interface remained at ~15–16 wt% and considered to be sufficient to reform a protective layer in the event of mechanical damage to the original. No additional chromium depletion of the alloy occurred during the 4-h deposition stage.

**Keywords** Pre-oxidation · Carbon deposition · Chromia · Stainless steel

---

✉ M. P. Taylor  
M.P.Taylor@bham.ac.uk

<sup>1</sup> The University of Birmingham, Birmingham B15 2TT, UK

<sup>2</sup> EDF Energy, Barnwood, Gloucester GL4 3RS, UK

## Introduction

It has been recognised for many years that selective pre-oxidation of chromium-bearing alloys to form a chromia layer reduces or eliminates carbon deposition and carburisation in CO<sub>2</sub>-based environments [1, 2]. This benefit has also been observed in the steam cracking process where the onset of coking was delayed by the formation of a chromia layer at the surface of alloys [3]. Studies to date have employed micrometre-thick chromia layers which can result in substantial depletion of chromium in the underlying alloy [1, 2, 4, 5]. Such depletion profiles are characteristic of the selective oxidation process [6] and can prejudice the ability of the alloy to reform a healing layer should the original layer crack or spall [7, 8].

The purpose of the present study was to examine the effect of thin sub-micrometre chromia layers on carbon deposition on a Nb-stabilised 20Cr25Ni austenitic stainless steel. It is known from previous studies on this alloy [2, 9] that such carbon deposition is filamentary in nature and is catalysed by nickel-rich metallic particles produced during the initial stages of oxidation in, typically, ethene-bearing CO<sub>2</sub>/1%CO gas. The catalytic nature of such particles has been well documented in the literature [10–14]. This process does not lead to carburisation of the underlying alloy as in “metal dusting” [15–17] but may be a precursor to this.

The aim of this paper is to present the results of a study designed to prevent the formation of the catalytic particles by the early development of a protective, continuous surface layer of chromia. The intention is to examine the efficacy of oxide layers appreciably thinner than those used previously [2, 4, 5]. The results presented here will find relevance in applications which may benefit from the formation of a highly protective oxide layer formed during a pre-oxidation heat treatment, e.g. solid state fuel cells and heat exchangers. The work here focuses on the effect of the pre-oxidising heat treatment on the composition of the initial oxide formed and also the effect this has on the early stages of exposure to an atmosphere with a high carbon activity. The presence or otherwise of filamentary carbon deposits is used as an indicator of the effectiveness of this approach in producing a highly protective continuous layer of chromia across the surface of the alloy.

## Experimental Procedures

A section of commercial alloy in the form of a can with a diameter of 15 mm and wall thickness of approximately 0.4 mm was supplied. The nominal composition of the alloy was 20.0Cr, 25.0Ni, 53.1Fe, 0.7Nb, 0.6Mn and 0.56Si wt%. The can was sectioned into approximately 15 mm long ring specimens using a slow speed saw and this was in turn sectioned into three samples of approximate final dimensions 15 mm by 10 mm. Great care was taken during the sectioning process to avoid stresses being induced from clamping of the can. Burrs produced during

the sectioning process were removed using 1200-grit SiC paper, thus removing any possible extraneous sources of particles that might catalyse the deposition process. The samples were cleaned in ethanol in an ultrasonic bath prior to being subjected to the standard heat treatment for this alloy, i.e. 930 °C for 30 min.

For the heat treatment process, the samples were placed in alumina boats and positioned in a controlled gas, heat treatment furnace with extraction. The rig was sealed and checked for gas tightness. All sections of the circuit of the rig were purged for a total of 2 h using a dry gas mixture of 5% H<sub>2</sub> in Ar at a flow rate of approximately 0.3 l min<sup>-1</sup>. Following this, the temperature of the furnace containing the samples was brought up to 930 °C, at a heating rate of 20 °C min<sup>-1</sup>. To introduce moisture into the gas mixture, the pipework had been split before entering the heat treatment furnace to provide two routes controlled by a valve, and this diverted the gas through a flask containing deionised water. It should be noted here that the bypass circuit and flask were included in the purging sequence. The valve was used to direct all or some of the gas through the flask, and in this way it was possible to control the moisture levels achieved. The moisture content of the gas was measured continuously during the heat treatment period using a Vaisala dew point and temperature transmitter DMT342 hygrometer sited at the entrance to the annealing furnace. The samples were held in this environment for 30 min, after which the alumina boat was moved, within the sealed furnace, to a forced cooled section and allowed to cool to room temperature before removal and storage.

Data on the moisture levels achieved are given in Table 1. The dew points recorded for each heat treatment were -13 °C, -41 °C and -53 °C. These represent the average levels achieved during the heat treatment with the variations shown in the table. These average dew point values will be used to identify each sample. Also included in Table 1 are the p<sub>H<sub>2</sub></sub>/p<sub>H<sub>2</sub>O</sub> ratios for each condition, using the H<sub>2</sub> concentration in the annealing gas, i.e. 50,000 vpm (5%), and the H<sub>2</sub>O reading, in ppm, from the hygrometer. The p<sub>O<sub>2</sub></sub> of each gas mixture can be calculated for the reaction:



according to:

$$p_{\text{O}_2} = \frac{p^2_{\text{H}_2\text{O}}}{p^2_{\text{H}_2}} \exp\left(\frac{\Delta G_A^\circ}{RT}\right) \quad (2)$$

where  $\Delta G_A^\circ$  is the standard free energy for the reaction in (A),  $R$  is the gas constant and  $T$  is temperature in K. The p<sub>O<sub>2</sub></sub>, which for the purpose of this work will

**Table 1** Moisture levels in heat treatment gas with calculated p<sub>O<sub>2</sub></sub> from Eq. 2

Dew point/°C	H <sub>2</sub> O/ppm	p <sub>H<sub>2</sub></sub> /p <sub>H<sub>2</sub>O</sub>	p <sub>O<sub>2</sub></sub>
-53	27 ± 3	2 × 10 <sup>3</sup>	6.1 × 10 <sup>-23</sup>
-41	100 ± 15	5 × 10 <sup>2</sup>	8.4 × 10 <sup>-22</sup>
-13	2030 ± 75	2.5 × 10 <sup>1</sup>	3.4 × 10 <sup>-19</sup>

be considered to be the oxygen activity, calculated in this manner using  $\Delta G_A^\circ$  data obtained from [18], for each of the heat treatment environments, is given in Table 1.

The dissociation oxygen activities of NiO, Cr<sub>2</sub>O<sub>3</sub> and Fe<sub>3</sub>O<sub>4</sub> are  $7.8 \times 10^{-17}$ ,  $2.7 \times 10^{-32}$ , and  $2.8 \times 10^{-22}$ , respectively, calculated for the pure substances [18]. The activities of the elements in the alloy will be less than unity so this approach provides a conservative estimate of the reactivity of the individual gas mixtures. From the calculated values given in Table 1, it can be seen that NiO is not expected to form in any of the three annealing gas mixtures used. However, Cr<sub>2</sub>O<sub>3</sub> is expected to form in all cases and Fe<sub>3</sub>O<sub>4</sub> is only expected to form in the gas mixture with the highest moisture content, i.e. the highest  $pO_2$ .

Following the oxidising heat treatments, the samples were moved within the furnace out of the hot section of the furnace and allowed to cool to room temperature under the flowing gas before removal. Selected samples were further exposed to an atmosphere of nominal composition 1%CO, 1000 vpm C<sub>2</sub>H<sub>4</sub>, balance CO<sub>2</sub> at 1 atmosphere total pressure at a temperature of 700 °C for 4 h. Details of the exposure protocol are as follows. The samples were placed in alumina boats and positioned within a purpose built rig at room temperature, and the rig is sealed and checked for gas tightness. The rig was purged with the same gas as before, i.e. 5% H<sub>2</sub> in Ar, for 2 h. The rig consisted of two furnaces in series. After the initial purge, the first furnace was brought up to 700 °C; this was followed, after a further 1 h purge, by the second furnace, also set to 700 °C. The first furnace housed titanium foil used to remove residual oxygen from the test gases and ensure a low  $pO_2$  was achieved. After this, the gases were swapped to the carbon depositing gas and held at 700 °C for 4 h. At the end of this time period, the gas was swapped back to 5% H<sub>2</sub> in Ar and the samples were cooled within the furnace. At all stages of the exposure, the flow rate of the gases was approximately 0.3 l min<sup>-1</sup>.

The samples were examined after the heat treatment stage and also after the final deposition exposure. Examination of the surfaces of the samples was performed using the JOEL 7000F Scanning Electron Microscope fitted with a Field Emission Gun (FEGSEM). This equipment has the capability of resolving the filamentary carbon fibres without the need for additional sample preparation, e.g. coating with a conductive layer. Cross sections were also prepared of each stage in the testing to provide information on the composition and thickness of the surface oxide and also record elemental depletion of the alloy. This analysis was achieved by taking cross sections using a dual-beam FEI Quanta 3D system consisting of a Focussed gallium Ion Beam (FIB) and a conventional field emission scanning electron microscope (SEM) column. Regions, characteristic of the surface of the samples, were selected, extracted and thinned by FIB. The initial stages of foil preparation used a 30-keV ion beam with the probe current reduced successively throughout the procedure, and a final polishing/cleaning was performed at 5 keV. The foils were examined using an FEI Tecnai F20 STEM equipped with an Oxford Instrument X-max SDD detector operating at 200 kV.

## Results

### Oxidising Heat Treatment

Figure 1 shows SEM images of the surface of the samples after the 30 min heat treatment at 930 °C with increasing levels of moisture. The image in Fig. 1a shows the effect on the surface of the alloy under dry conditions. The machining marks are clearly visible with no obvious surface oxide formed. On inclusion of moisture to the 5% H<sub>2</sub> in Ar heat treatment gas, a scale consisting of very fine oxide grains with pores in the order of 100 nm was formed on the surface of the samples, as shown in Fig. 1b. With increasing moisture levels, the definition of the machining marks reduced until at the highest level used here, i.e. with a dew point of -13 °C, few marks were discernible, as shown in Fig. 1d. On inspection,

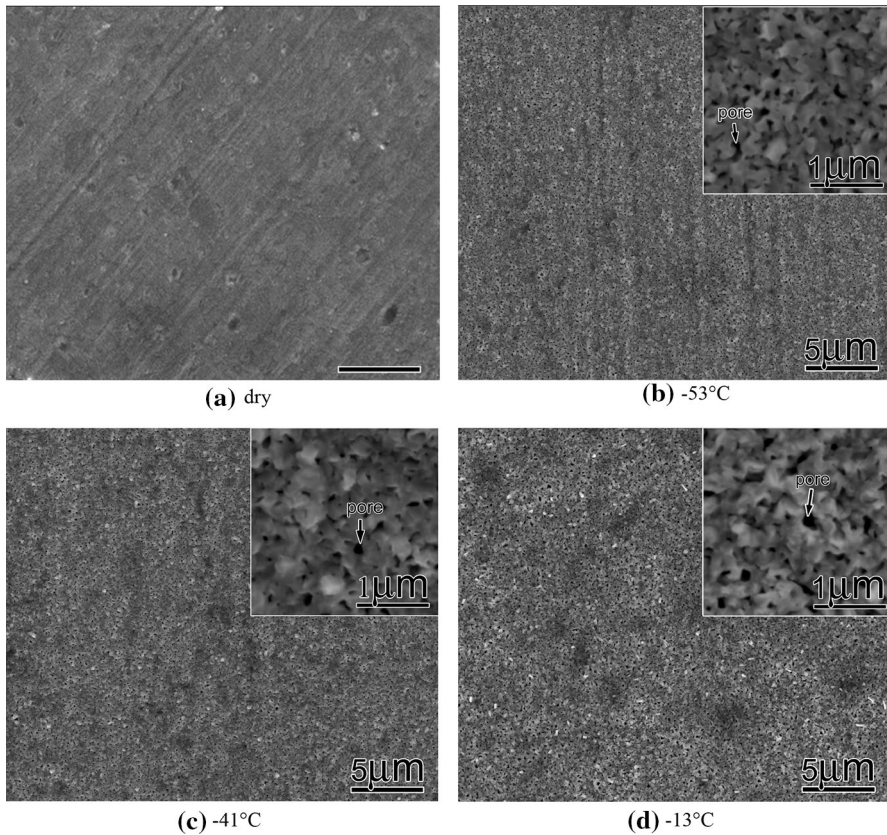


**Fig. 1** SEM images of the surfaces of the samples following the heat treatment in 5% hydrogen in argon at 930 °C for 30 min with increasing moisture level (dew point): **a** in dry gas, **b** -53 °C, **c** -41 °C, **d** -13 °C

it appeared that the pore size present within the oxide layer was largest when the moisture content was highest.

Figure 2 shows a series of montages of high-angle annular dark field (HAADF) STEM images obtained from FIBbed foils of cross sections through the samples shown in Fig. 1b–d. The images revealed that on each sample a thin external layer of oxide, in dark contrast, had formed on the lighter contrast alloy beneath. In all samples, the effect of the heat treatment on the alloy was to produce a single-phase microstructure of grains containing twins and precipitates. Two types of precipitates were identified, discernible by contrast. A typical EDS spectrum obtained from a light contrast precipitate indicated that it was a Nb-rich carbide, as shown in Fig. 3a. Electron diffraction was used to identify the crystal structure of the carbide, and the diffraction patterns taken from three different zone axes are shown in Fig. 3b–d, confirming that the particle was an fcc NbC with a lattice parameter  $a=0.44$  nm [19]. The nanometre-sized darker contrast precipitates (Fig. 4a, b) were shown, by

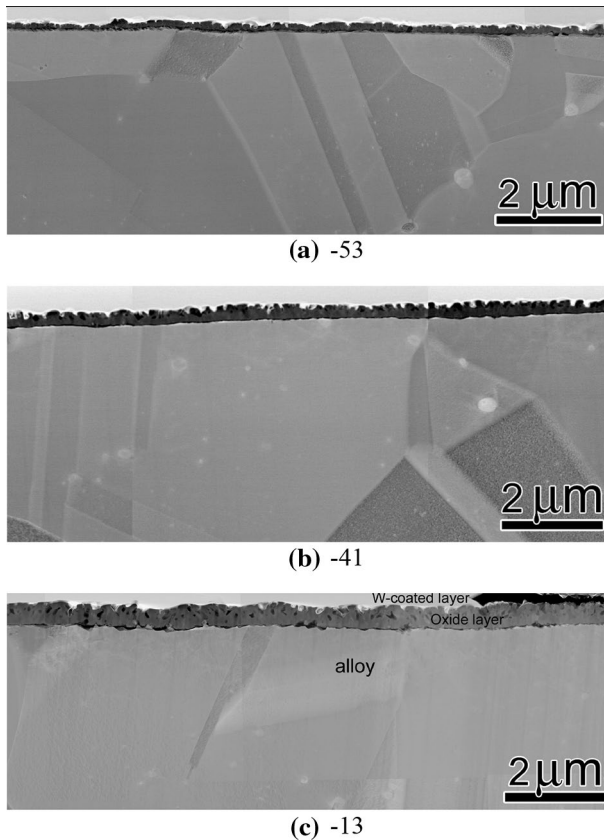


**Fig. 2** HAADF STEM images of the cross sections from the pre-oxidised samples exposed to the gas with moisture levels of: **a** – 53 °C, **b** – 41 °C, **c** – 13 °C, showing the microstructure of the alloy and the formation of a surface oxide whose thickness increases with increasing level of moisture

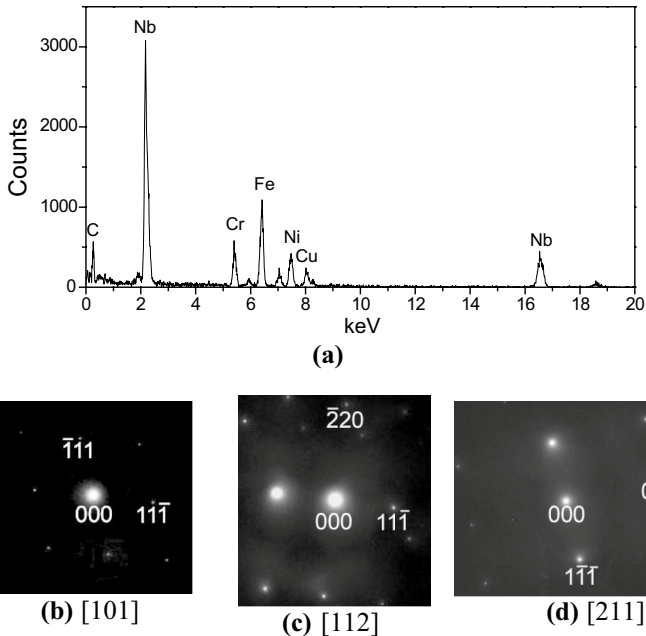


**Fig. 3** **a** EDS spectrum from a light contrast particle (as seen in Fig. 2) with selected area diffraction patterns taken along the **b** [101], **c** [112], **d** [211] directions, consistent with the fcc structure of NbC

EDS linescans, to be (Al, Mn)-rich oxides, as shown in Fig. 4c–e. In addition, a very thin Si-rich layer was found surrounding the (Al, Mn)-oxide particles, as shown in Fig. 4f. The oxygen linescans showed this layer to be a Si-rich oxide.

Examination of the oxide formed under the three moisture containing heat treatment conditions revealed that the thickness increased with increasing moisture content in the annealing gas, as shown in Table 2. Examination of the cross sections in Fig. 2 shows that the outer contour of the oxide exposed to the gas with dew point of  $-41\text{ }^{\circ}\text{C}$  resembles crenulations. It is also noted that in the sample exposed to the highest moisture level, i.e. with a dew point of  $-13\text{ }^{\circ}\text{C}$ , a series of pores exist within the oxide at about the same distance from the alloy as the crenulations formed under the gas with a dew point of  $-41\text{ }^{\circ}\text{C}$ . This suggested that the oxide was growing by outward cationic diffusion and the crenulations and pores were due to differences in the growth rates of adjacent oxide grains; lateral grown of the crystals with the preferred growing direction perpendicular to the alloy surface enclosed any slower growing oxide adjacent grains producing the series of pores within the structure. Also recorded in Table 2 are the depths of depletion for Cr from the alloy under each of the three pre-oxidising heat treatments. These measurements are taken from EDS Cr concentration profiles such as those shown in Fig. 5 for the three oxidising heat treatments: (a)  $-53\text{ }^{\circ}\text{C}$ , (b)  $-41\text{ }^{\circ}\text{C}$  and (c)  $-13\text{ }^{\circ}\text{C}$ . The depth is measured from the alloy/oxide interface to the position where there is no measurable Cr depletion. As shown in Fig. 5, the concentration of Cr in the alloy immediately beneath the oxide in each case is approximately (a) 16, (b) 17 and (c) 15 at.%, which is at the

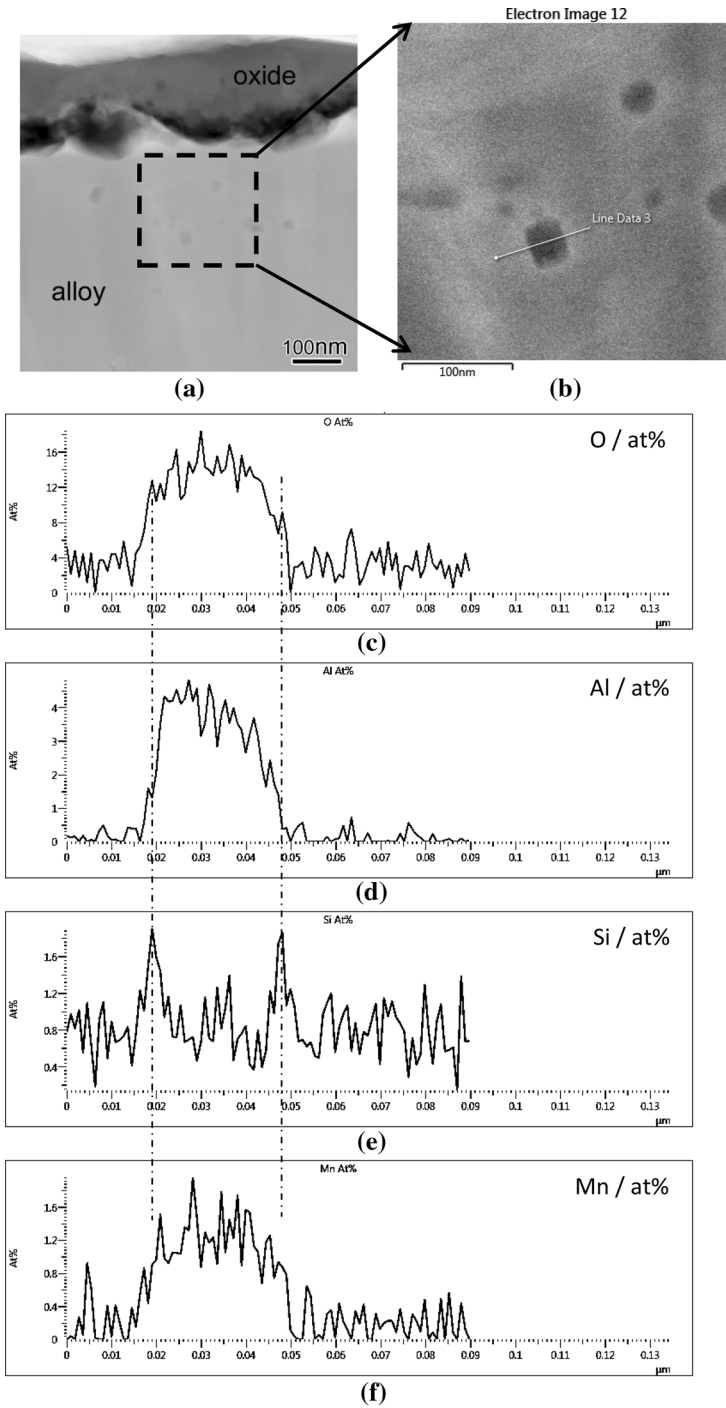


**Fig. 4** STEM images of dark contrast nanosize particles in the alloy (a) and magnified in b. EDS line-scans of c O, d Al, e Si, f Mn taken from location indicated in b

**Table 2** Thickness of oxide layers and depth of chromium depletion related to pre-oxidation dew point, after the heat treatment and subsequent deposition stage

Dew point/°C		−53 °C	−41 °C	−13 °C
Pre-oxidation heat treatment	Oxide thickness (nm)	125 ± 25	265 ± 25	380 ± 30
	Cr depletion depth (μm) <sup>a</sup>	1.3	2.5	3.0
Post deposition	Oxide thickness (nm)	140 ± 20	270 ± 30	390 ± 30
	Cr depletion depth (μm) <sup>a</sup>	1.4	2.4	3.1

<sup>a</sup>Chromium depletion depth was the mean value from three measurements

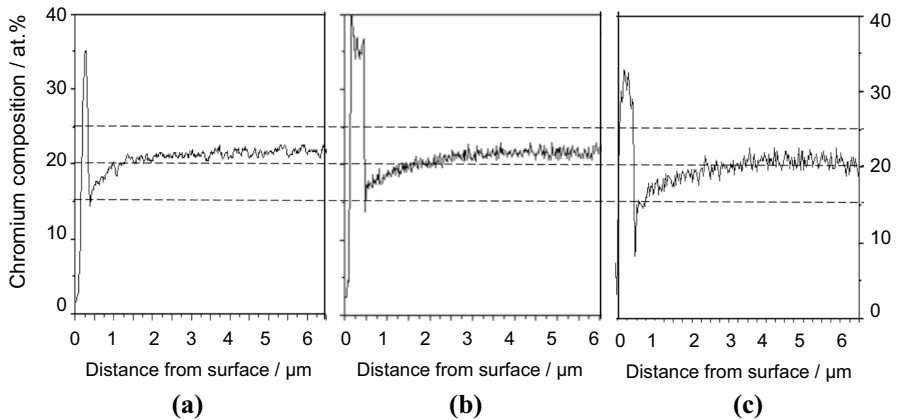


**Fig. 5** Compositional profiles of chromium taken from cross sections through samples post-heat treatment exposed to gases with dew points of **a** −53 °C, **b** −41 °C, **c** −13 °C, showing the depth of depletion in each case and also that the concentration of chromium within the alloy beneath the oxide is approximately 16, 17 and 15 at.%, respectively

minimum concentration level of approximately 16 at.% previously determined for this alloy to enable the reformation of a protective chromia layer should the TGO be damaged [20]. In addition, no evidence of enhanced Cr depletion was found at the grain boundaries.

EDS mapping was used to reveal the elemental distribution in the oxide layers. Figure 6 shows elemental maps from the sample exposed to the heat treatment gas with a dew point of −13 °C. The maps indicate that the oxide consisted of mainly Cr with grains of (Cr, Mn) spinel. A thin and continuous Si-rich oxide layer of approximately 100 nm was also present, located between the Cr-rich oxide and the alloy. The beneficial effect of the formation of a Si-rich layer on the early establishment of a Cr<sub>2</sub>O<sub>3</sub> layer in this alloy has been reported previously [21, 22]. EDS linescans, as shown in Fig. 7, across the same sample confirmed the composition of the oxide, i.e. grains of Cr<sub>2</sub>O<sub>3</sub> with Mn concentrated at the inner and outer surfaces of the layer. The inclusion of Mn in the surface oxide is reflected in the depletion of this element from the underlying alloy, as shown in Fig. 7. The formation of a Si-rich layer in contact with the

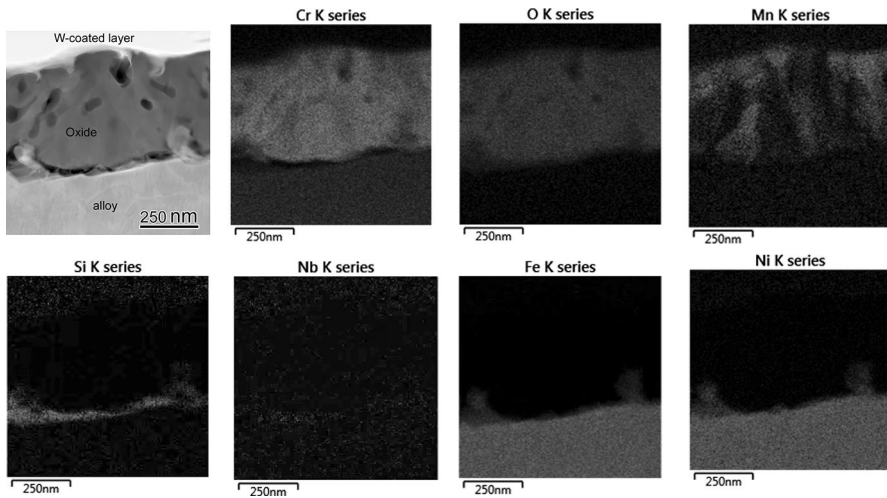


**Fig. 6** HAADF image and EDS maps of the oxide layer formed on the sample exposed to the annealing gas with a dew point of  $-13\text{ }^{\circ}\text{C}$ , showing that the oxide is rich in Cr and Mn and that a Si-rich oxide has formed at the interface between the oxide and the alloy

alloy and also a very thin Nb-rich oxide layer at the same site was also revealed. From examination of the EDS map for Nb in Fig. 6, it can be assumed that the Nb concentrated at the surface was not a continuous layer. Diffraction patterns taken of the main oxide, as shown in Fig. 8, confirmed the presence of hexagonal  $\text{Cr}_2\text{O}_3$  with lattice parameters  $a = 0.495\text{ nm}$  and  $c = 1.36\text{ nm}$  [23]. In order to clarify whether the (Cr, Mn)-oxide was a different phase or a manganese-doped chromia, spot EDS and electron diffraction were performed. Spot EDS analysis showed that the Mn content in the (Cr, Mn)-oxide was up to 13.4 at.%, which is related to the size of (Cr, Mn)-oxide (i.e. ratio of the (Cr, Mn)-oxide size to the foil thickness). The composition of the typical (Cr, Mn)-oxide examined in this work, with a high Mn content, was: 13.4 Mn, 31.6 Cr and 55 O at.%. Diffraction patterns taken are shown in Fig. 9, which confirm that the (Cr, Mn)-oxide is the fcc  $\text{MnCr}_2\text{O}_4$  with a lattice parameter of  $a = 0.84\text{ nm}$  [24].

The oxide type and distribution were consistent in all samples and thus found to be independent of the moisture level of the gases used. It should be noted that no Fe-rich oxides or (Ni, Fe)-rich particles were found in these samples. The oxides present and the absence of Fe and Ni oxides are consistent with the predictions of oxide formation under the gas compositions used. There was some evidence of localised enrichment of Fe at the alloy oxide surface which is consistent with the selective oxidation process, as shown in Fig. 6. The concentration of Cr within the alloy is sufficient, after the pre-oxidising heat treatment, to form a healing layer of  $\text{Cr}_2\text{O}_3$  should the oxide be damaged. In this regard, the oxidation behaviour of the alloy would not be compromised by the pre-oxidation treatment.

**Fig. 7** STEM image and EDS line scans showing elemental profiles from the sample exposed to the annealing gas with a dew point of  $-13\text{ }^{\circ}\text{C}$ , confirming EDS mapping results in that the main oxide layer is composed of Cr-oxide and (Cr,Mn)-oxide, and a thin Si-rich oxide layer is located at the oxide/alloy interface, Cr depletion from the alloy with a value of  $\sim 14\text{ at.}\%$  at the surface, Nb enrichment at oxide/alloy interface and (arrowed) Nb carbide particle. Also shown are horizontal dashed lines on individual scans indicating the starting composition of the alloy for that element

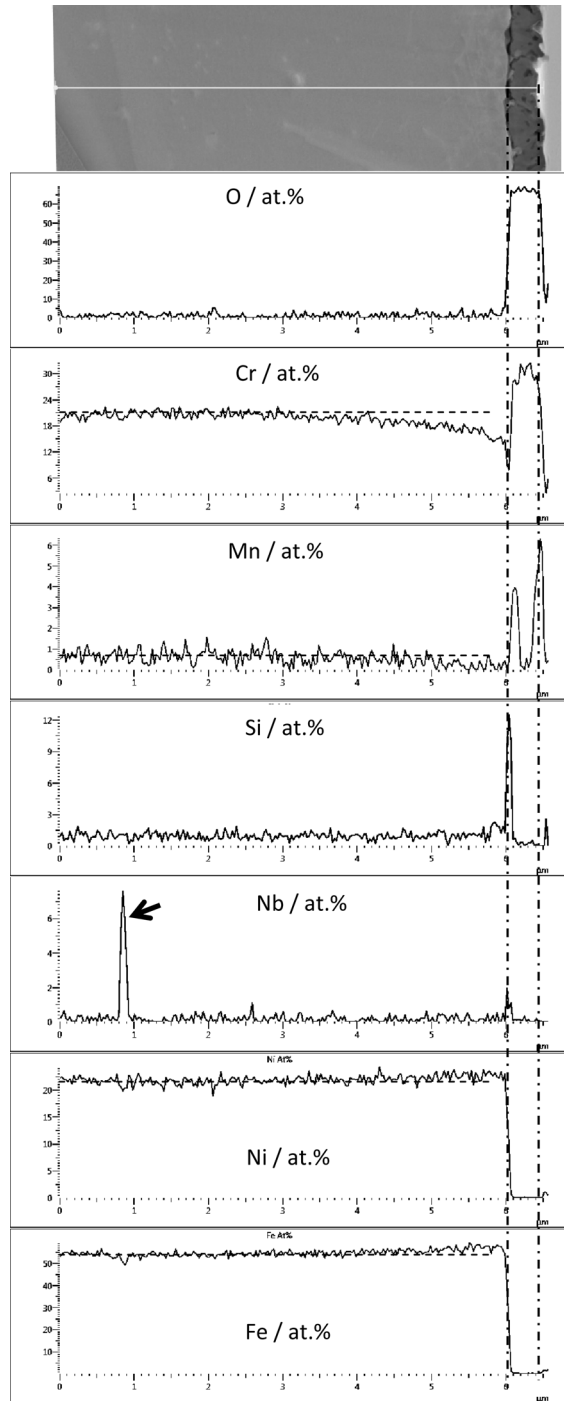


**Fig. 8** Diffraction pattern of  $\text{Cr}_2\text{O}_3$  taken along  $[10\bar{1}1]$  zone axis formed on the sample exposed to the gas with a dew point of  $-13^\circ\text{C}$

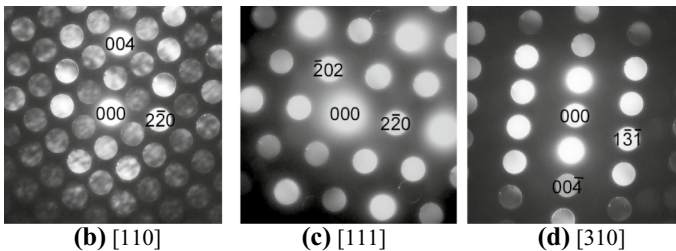
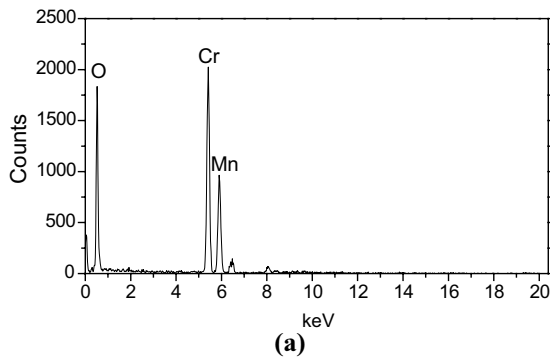
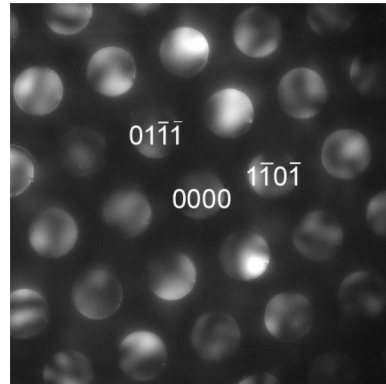


**Fig. 9** EDS spectrum from  $\text{MnCr}_2\text{O}_4$  grain located in top right in Fig. 6 showing (a), diffraction patterns of  $\text{MnCr}_2\text{O}_4$  taken along  $[110]$  (b),  $[111]$  (c) and  $[310]$  (d) zone axis, respectively, formed on the sample exposed to the gas with a dew point of  $-13^\circ\text{C}$

## Carbon Deposition

The effect of exposure to the carbon depositing gas of a sample of the alloy that had undergone the conventional heat treatment under an inert dry gas is shown in Fig. 10. Filamentary carbon deposits were formed on the surface of the alloy associated with the centres of the large grains during the early stages of exposure. These locations have been shown previously to be the sites of mixed oxide formation containing the Ni-rich catalytic particles [2, 25]. Figure 11 shows the

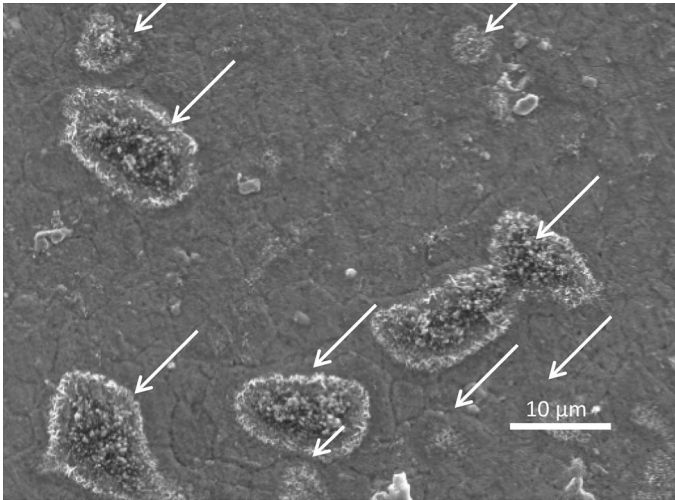


**Fig. 10** SEM image of the surface of a section of the alloy heat-treated in a dry inert gas and after exposure to the depositing gas for 4 h at 700 °C showing islands of filamentary carbon deposits, indicated by arrows

dramatic difference the formation of a surface oxide during the heat treatment stage had on the carbon deposition process. No islands of filamentary carbon deposits were found on the surface of any of the samples subjected to oxidising heat treatment. Carbon fibres were found on the surface of the sample exposed to the gas with the lowest dew point, i.e.  $-53$  °C, associated with major defects on the surface of the alloy resulting from the machining processes, as shown in Fig. 11a. These carbon deposits were far less extensive and less dense than those seen in Fig. 10. The sample exposed to the heat treatment gas with a dew point of  $-41$  °C produced fewer carbon filaments, as shown in Fig. 11b, and none were observed on the sample exposed to the annealing gas with the highest dew point and thus the thickest oxide, i.e.  $-13$  °C, as shown in Fig. 11c. On samples where carbon fibres were identified, bright contrast metallic particles were often observed at the tips. EDS analysis yielded significant carbon and nickel peaks associated with the particles, as shown in Fig. 11d, as well as Cr and O from the underlying oxide. Previous work has shown clearly that these particles are Ni or Ni-rich and encased in C [9, 25, 26]. The location of the carbon fibres on the surface of the alloy suggests that the defects on the surface caused during the machining process can be sites of Ni particle formation.

Cross-sectional examination of the samples showed that the surface oxide had not increased significantly in thickness during the carbon deposition exposure stage, as shown in Table 2. The increase noted was between 5 and 15 nm which was within the standard deviation of oxide thickness measurements. Also shown in Table 2 are the Cr depletion depths where again no significant difference was found compared to the post-heat treatment stage. EDS analysis of the oxide showed that no

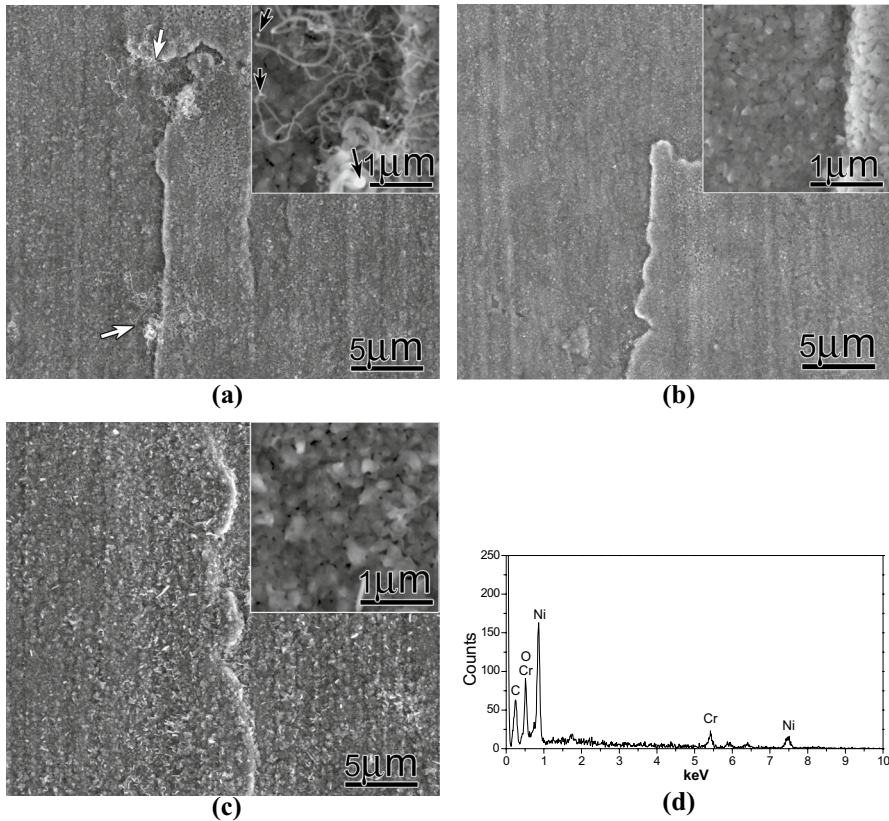


**Fig. 11** SEM images of the surface of the samples exposed to an inert gas with increasing moisture content (with dew point of **a**  $-53$  °C, **b**  $-41$  °C, **c**  $-13$  °C) during heat treatment and following exposure to a carbon deposition gas for 4 h at 700 °C. Note: in Fig. 10a, white arrows show carbon deposits, black arrows, top left inset, showing Ni-rich particles, **d** EDS trace from particle

compositional changes had occurred to the oxide during the carbon deposition stage, compare Fig. 12 to Figs. 6 and 7, and significantly, no Ni-rich particles had formed.

## Discussion

The catalytic nature of Ni-rich particles and their role in carbon deposition has been well documented [2, 11]. A mechanism for the production of nanometre-sized particles from the 20Cr:25Ni austenitic stainless steel has been proposed earlier [2]. This involved the selective, internal oxidation of Fe and Cr from the alloy under low oxygen environments. Under these conditions, Ni would not oxidise but instead becomes concentrated as particles within the mixed oxides of Cr and Fe. On exposure to a gas with a high carbon activity, filamentary carbon deposits form on the surface of the alloy, preferentially at the centre of exposed grains. It has been shown

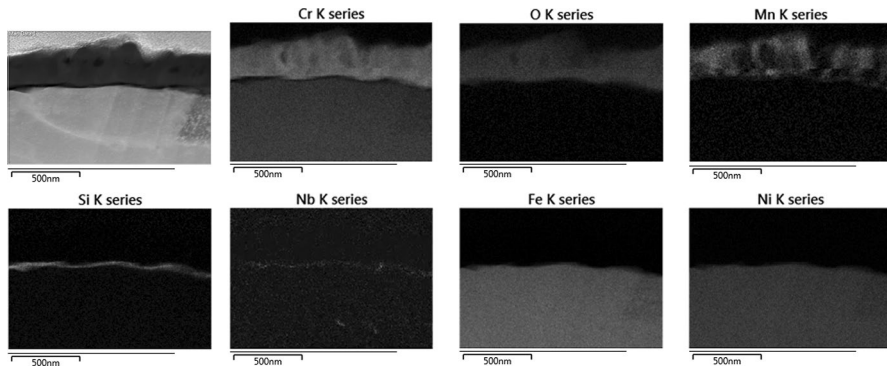


**Fig. 12** STEM image and EDS maps of a cross section taken from the sample subjected to the heat treatment with the highest moisture content (dew point of  $-13\text{ }^{\circ}\text{C}$ ) after carbon deposition, indicating that the oxide was composed of Cr and mixed (Cr and Mn) spinel, with a Si-rich oxide at the interface with the alloy as well as low levels of Nb at that interface

more recently that these regions of the grains experience greater internal oxidation [25]. The results presented here demonstrate a route that prevents this mechanism occurring by the early formation of a surface chromia layer.

By careful manipulation of the moisture content of the heat treatment gas, it has been shown here that it is possible to form a thin, surface layer of a protective chromium oxide which included grains of chromium/manganese spinel. Similar findings have been reported in Ref. [27] where the effect of  $p\text{O}_2$  on the composition of the surface oxide was explained in terms of the influence of the  $p\text{O}_2$  on the solubility of Mn in  $\text{Cr}_2\text{O}_3$ . Improved scale adhesion was also noted in that work. The conditions shown in this work ensure that the oxidation of Fe and Ni was not thermodynamically favourable although Si was and thus a layer of silica formed at the interface between the  $\text{Cr}_2\text{O}_3$  and the alloy. As a consequence, no metallic particles were formed. Exposure of these pre-oxidised samples to the high carbon activity gas mixture demonstrated the effectiveness of this approach in significantly reducing and ultimately preventing the deposition of filamentary carbon. The level of reduction was shown to be dependent on the thickness of the surface oxide as a level of porosity existed within the oxide formed. The presence of carbon fibres on the thinner oxide formed on exposure to the gas with a dew point of  $-53\text{ }^{\circ}\text{C}$  suggested that access of the gas was still possible through to the alloy underneath, probably via the network of pores observed. Figure 13 shows a high-magnification image of the surface of a sample with carbon fibres anchored to the pores of the oxide. It was found that a surface oxide of approximate thickness 350 nm resulted in complete inhibition in the formation of filamentary carbon deposits. Significantly, the previously observed islands of copious filamentary carbon deposits, which formed on the samples heat-treated under a dry inert atmosphere, were absent in all pre-oxidised samples. Isolated carbon fibres were seen on the sample with the thinnest surface oxide formed, associated with surface defects produced during the machining process.

The composition of the surface oxide formed during the oxidising heat treatment has been confirmed by TEM cross-sectional analysis to be composed of  $\text{Cr}_2\text{O}_3$  with

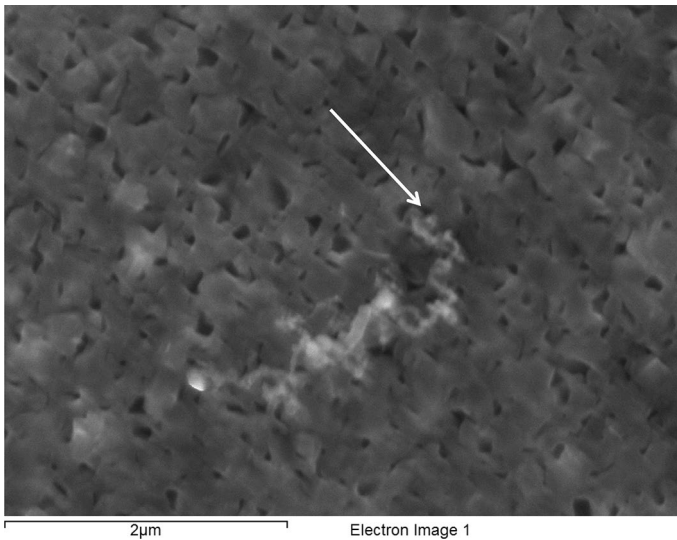


**Fig. 13** SEM image of the surface of a sample exposed to the pre-oxidising heat treatment with a dew point of  $-53\text{ }^{\circ}\text{C}$  and followed by exposure to the carbon depositing gas for 4 h at  $700\text{ }^{\circ}\text{C}$  showing carbon fibres anchored to the sample at a pore, indicated by the arrow

grains of a (Cr, Mn) spinel. Underlying these, a thin layer of Si was identified as was an enhancement of Nb. Significantly, no oxides of Ni or Fe nor metallic particles of these elements were found within the oxide. Calculation of the activities of the oxygen in the annealing gases amply explains the oxides observed, as oxides of Si, Cr, Mn and Nb are all thermodynamically stable under the conditions used here. It could be expected that the alloy heat-treated using the gas with the highest moisture content and thus highest oxygen activity would form  $\text{Fe}_3\text{O}_4$ . The lack of evidence of iron oxides in the surface oxide would suggest that the more protective oxides form rapidly and dominate the surface, thereby reducing the oxygen activity at the oxide/alloy interface still further to that in equilibrium with those more stable oxides.

The uniformity in the thickness and composition of the oxide across the surface and the lack of evidence of any enhanced grain boundary depletion shows that the conditions used for the oxidising heat treatment favour the formation of a uniform oxide across the whole surface of the alloy. This is in contrast to that observed for this alloy when exposed to lower temperatures,  $500\text{--}700\text{ }^{\circ}\text{C}$ , where relatively faster grain boundary diffusion compared with that in the lattice results in the formation of a protective surface oxide of chromium at the emerging grain boundaries which grow laterally [2, 6, 9, 25] until coverage of the surface is achieved [28]. Once an oxide has been established on the surface of the alloy, the continued growth will be dominated by diffusion through the oxide and, predominantly, via grain boundaries [29–32].

It was found that the thickness of the surface oxide was related to the oxygen activity of the annealing gas. Rate constants, assuming parabolic growth, were determined from the oxide thicknesses formed over the 30 min heat treatment and

are plotted in Fig. 14. Also included is a value obtained from Ref. [5] for the same alloy but under 2% H<sub>2</sub>O in H<sub>2</sub> for 60 min. It is acknowledged that the data are based on limited data, but it demonstrates the increase in oxidation rate with increasing oxygen content of the annealing gas. The broken line included in Fig. 14, with a slope of 3/16, is fitted to the results at the three highest oxygen activity values and is the dependence expected for oxide growth by Cr diffusion via cation vacancies. It is possible that the apparent dependence at the oxygen activity derives not from an effect on cation vacancy concentration but on a reduction in the supply of oxygen.

## Conclusion

It has been known for many years that the formation of a chromia layer of a few micrometres in thickness can protect the underlying alloy from carbon deposition and carburisation in atmospheres of high carbon activity ( $> 1$ ). This pre-oxidation procedure can lead to substantial and deleterious Cr depletion of the underlying alloy, however. The purpose of the present work was to examine whether much thinner oxide layers could also provide useful protection against carbon deposition.

A technique has been developed that produces adherent layers of chromia, together with crystals of MnCr<sub>2</sub>O<sub>4</sub>, on an austenitic steel pre-oxidised at 930 °C in Ar/H<sub>2</sub>/H<sub>2</sub>O mixtures. By control of the moisture content of this gas, oxide layer thicknesses in the range 125 nm to 350 nm were produced. This resulted in depletion of Cr from the alloy, but the remaining concentration was sufficient to ensure rehealing occurred if the surface oxide was damaged.

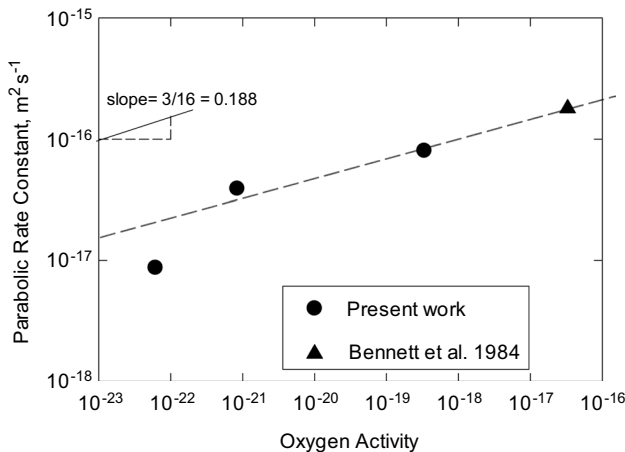


**Fig. 14** Plot of parabolic rate constants against oxygen activity determined from the oxide thicknesses formed during the heat treatments at 930 °C in the present work (circles). Also shown (triangle) is the estimate of the parabolic rate constant from the work of Bennett et al. [5] for a 930 °C anneal on the same steel but a higher oxygen activity. The broken line with a slope of 3/16 is fitted to the results at the three highest oxygen activity values and is the dependence expected for oxide growth by Cr diffusion via cation vacancies

The ability of these layers to protect against carbon deposition was examined by exposure to a gas mixture of CO<sub>2</sub>/1%CO/1000 vppmC<sub>2</sub>H<sub>4</sub> at 700 °C for 4 h. It has been shown that a significant reduction in filamentary carbon deposition was achieved with surface oxides as thin as 125 nm, although isolated carbon fibres were found associated with machining defects and pores in the oxide layer. Total suppression of carbon formation was achieved on the sample which possessed an oxide thickness of approximately 350 nm.

**Acknowledgements** The authors are grateful to EDF Energy for their financial support for this work. The support provided by the Centre for Electron Microscopy at the University of Birmingham is also acknowledged.

**OpenAccess** This article is distributed under the terms of the Creative Commons Attribution 4.0 International License (<http://creativecommons.org/licenses/by/4.0/>), which permits unrestricted use, distribution, and reproduction in any medium, provided you give appropriate credit to the original author(s) and the source, provide a link to the Creative Commons license, and indicate if changes were made.

## References

1. G. W. Horsley and J. A. Cairns, *Applications of Surface Science* **18**, 273 (1984).
2. G. R. Millward, H. E. Evans, M. Aindow, and C. W. Mowforth, *Oxidation of Metals* **56**, 231 (2001).
3. P. R. S. Jackson, D. J. Young, and D. L. Trimm, *Journal of Materials Science* **21**, 4376 (1986).
4. J. E. Bainbridge, G. W. Horsley, J. A. Cairns, and P. Campion, UK patent: GB 2 097 821A. Carbon Deposition Inhibition (1982).
5. M. J. Bennett, J. A. Desport, and P. A. Labun, *Oxidation of Metals* **22**, 291 (1984).
6. H. E. Evans, D. A. Hilton, and R. A. Holm, *Oxidation of Metals* **10**, 149 (1976).
7. H. E. Evans, A. T. Donaldson, and T. C. Gilmour, *Oxidation of Metals* **52**, 379 (1999).
8. P. Huczowski, N. Christiansen, V. Shemet, J. Piron-Abellan, L. Singheiser, and W. J. Quadakkers, *Materials and Corrosion* **55**, 825 (2004).
9. G. R. Millward, H. E. Evans, I. P. Jones, and C. D. Eley, *Materials at High Temperature* **20**, 535 (2003).
10. P. A. Tesner, E. Y. Robinovich, I. S. Rafalkes, and E. F. Arefieva, *Carbon* **8**, 435 (1970).
11. C. Park and R. T. K. Baker, *Journal of Catalysis* **190**, 104 (2000).
12. M. S. Kim, N. M. Rodriguez, and R. T. K. Baker, *Journal of Catalysis* **134**, 253 (1992).
13. V. Z. Mordkovich, E. A. Dolgova, A. R. Karaeva, D. N. Kharitonov, I. A. Maslov, A. A. Kamenev, and V. F. Tretjakov, *Carbon* **45**, 62 (2007).
14. T. Baird, J. R. Fryer, and B. Grant, *Carbon* **12**, 591 (1974).
15. H. J. Grabke, R. Krajak, and J. C. Nava Paz, *Corrosion Science* **35**, 1141 (1993).
16. D. J. Young, J. Zhang, C. Geers, and M. Schuetze, *Materials and Corrosion* **62**, 7 (2011).
17. J. Zhang, P. Speck, and D. J. Young, *Oxidation of Metals* **77**, 167 (2012).
18. I. Barin, O. Knacke, *Thermochemical Properties of Inorganic Substances* (Springer, Berlin, 1973).
19. E. K. Storm and N. H. Krikirian, *The Journal of Physical Chemistry*; **63**, 1747 (1959).
20. H. E. Evans, D. A. Hilton, R. A. Holm, and S. J. Webster, *Oxidation of Metals*. **14**, 235 (1980).
21. R. C. Lobb, J. A. Sasse, and H. E. Evans, *Materials Science and Technology* **5**, 828 (1989).
22. M. J. Bennett, M. R. Houlton, and R. W. M. Hawes, *Corrosion Science* **22**, 111 (1983).
23. S. Greenwald, *Nature* **168**, 379 (1951).
24. S. J. Zheng, Y. J. Wang, B. Zhang, Y. L. Zhu, C. Liu, P. Hu, and X. L. Ma, *Acta Materialia* **58**, 5070 (2010).
25. M. P. Taylor, H. E. Evans, P. Smith, R. Ding, Y. L. Chiu, S. Rai, B. Connolly, N. Smith, L. Pearson, and C. W. Mowforth, *Oxidation of Metals* **87**, 667 (2017).
26. S. Rai, M. P. Taylor, Y. L. Chiu, H. E. Evans, B. J. Connolly, N. Smith, and C. W. Mowforth, *Materials Characterization*. **144**, 505 (2018).
27. J. Zurek, D. J. Young, E. Essuman, M. Hansel, H. J. Penkalla, L. Niewolak, and W. J. Quadakkers, *Materials Science and Engineering A* **447**, 259 (2008).
28. P. W. G. Simpson and H. E. Evans, *British Nuclear Energy Society* 265 (1985).

29. A. Atkinson and R. I. Taylor, in *Transport in Nonstoichiometric Compounds*, eds. G. Simkovich, V. S. Srubican (Plenum Publishing Corporation, New York, 1985) p. 285.
30. A. C. S. Sabioni, A. M. Huntz, F. Millot, and C. Monty, *Philosophy Magazine A* **66**, 361 (1992).
31. A. Holt and P. Kofstad, *Solid State Ionics* **69**, 137 (1994).
32. P. Kofstad, *Oxidation of Metals* **44**, 3 (1995).